

Site-substitution in GdMnO_3 : effects on structural, electronic and magnetic properties

Sudipta Mahana^{1,2,†}, Bipul Rakshit³, Pronoy Nandi^{1,2}, Raktima Basu⁴,
Sandip Dhara⁴, U. Manju⁵, Subhendra D. Mahanti⁶ and D. Topwal^{1,2,*}

¹*Institute of physics, Sachivalaya Marg, Bhubaneswar - 751005, India*

²*Homi Bhabha National Institute, Training School Complex, Anushakti Nagar, Mumbai - 400085, India*

³*Center for Superfunctional Materials, Ulsan National Institute of Science and Technology, Ulsan - 44919, South Korea*

⁴*Surface and Nanoscience Division, Indira Gandhi Centre for Atomic Research, HBNI, Kalpakkam - 603102, India*

⁵*CSIR -Institute of Minerals and Materials Technology, Bhubaneswar - 751013, India*

⁶*Department of Physics and Astronomy, Michigan State University, East Lansing, Michigan 48824, USA*

We report on detailed structural, electronic and magnetic studies of $\text{GdMn}_{1-x}\text{Cr}_x\text{O}_3$ for Cr doping levels $0 \leq x \leq 1$. In the solid solutions, the Jahn-Teller distortion associated with Mn^{3+} ions gives rise to major changes in the bc -plane sub-lattice and also the effective orbital ordering in the ab -plane, which persist up to the compositions $x \sim 0.35$. These distinct features in the lattice and orbital degrees of freedom are also correlated with bc -plane anisotropy of the local Gd environment. A gradual evolution of electronic states with doping is also clearly seen in O K -edge x-ray absorption spectra. Evidence of magnetization reversal in field-cooled-cooling mode for $x \geq 0.35$ coinciding the Jahn-Teller crossover, suggests a close correlation between magnetic interaction and structural distortion. These observations indicate a strong entanglement between lattice, spin, electronic and orbital degrees of freedom. The nonmonotonic variation of remnant magnetization can be explained by doping induced modification of magnetic interactions. Density functional theory calculations are consistent with a layer-by-layer type doping with ferromagnetic (antiferromagnetic) coupling between Mn (Cr) ions for intermediate compound ($x = 0.5$), which is distinct from that observed for the end members GdMnO_3 and GdCrO_3 .

I. INTRODUCTION

Functional oxides with perovskite structures (ABO_3) are very active research area not only due to their potential technological applications but also for their fundamental importance in basic scientific research. An unusual aspect of perovskites is their ability to incorporate almost every element of the periodic table at the A and B sites due to their capacity to accommodate various structural distortions¹. External parameters like temperature, pressure and chemical compositions, can also drive such distortions, which leads to an extraordinary richness of physical properties within the family of perovskites. Structural distortions in perovskites are mainly associated with three main features with respect to their ideal cubic structure:¹⁻³ (i) rotation (tilt) of BO_6 octahedra, (ii) polar cation displacements, which often lead to ferroelectricity, and (iii) distortions of the octahedra, such as the Jahn-Teller (JT) distortion.

The rare-earth manganites (RMnO_3) invoked great interest owing to the JT character of Mn^{3+} ions ($t_{2g}^3 e_g^1$), exhibiting orbital ordering along with highly anisotropic Mn-O bond lengths⁴. A complex interplay among the spin, orbital and lattice degrees of freedom has led to a large number of intriguing physical properties in RMnO_3 such as colossal magnetoresistance⁵, charge and orbital ordering⁶⁻⁸, metal-insulator transition^{9,10}, complex spin structures¹¹, multiferroic properties with significant magnetoelectric coupling¹². In contrast to Mn^{3+} , Cr^{3+} is JT inactive ion because of having completely empty e_g orbitals and therefore the oxygen octahedra are more regular. However, most of the members of RCrO_3 have been reported to be multiferroic materials at considerable high temperature^{13,14}. Additionally, RCrO_3 systems are of great interest as these exhibit complex magnetic properties such as spin-reorientation (SR), spin-flipping

(SF) and temperature induced magnetization reversal (TMR) etc.¹⁵⁻¹⁷

GdMnO_3 with the orthorhombic $Pbnm$ structure, exhibits incommensurate sinusoidal magnetic structure arising from competing nearest-neighbor ferromagnetic (NN-FM) and next-nearest-neighbor antiferromagnetic (NNN-AFM) interaction followed by a canted- A -type ordering in the Mn-sublattice^{11,18}. Additionally, a low temperature ferroelectric ordering is established, caused by Gd^{3+} - Mn^{3+} spin interactions and/or lattice distortions associated with magnetic field-induced spin rearrangements^{19,20}. GdCrO_3 is one of the G -type antiferromagnetic (AFM) RCrO_3 compounds, exhibiting extremely rich magnetic properties like TMR, SF, SR and others¹⁵. It has non-centrosymmetric $pnm2_1$ structure, associated with the ferroelectric transition concurrent to Cr magnetic ordering temperature with significant magnetoelectric coupling^{13,14}. Although the parent compounds without doping are well investigated, the doped solid solution $\text{GdMn}_{1-x}\text{Cr}_x\text{O}_3$ is largely unexplored²¹. Various interesting properties have been reported in similar type of mixed cation compositions such as $\text{DyMn}_{1-x}\text{Fe}_x\text{O}_3$ ²², $\text{LaMn}_{1-x}\text{Fe}_x\text{O}_3$ ²³, $\text{TbMn}_{1-x}\text{Fe}_x\text{O}_3$ ²⁴, $\text{YbMn}_{1-x}\text{Fe}_x\text{O}_3$ ²⁵, $\text{TbMn}_{1-x}\text{Cr}_x\text{O}_3$ ²⁶ and others. This has motivated us to investigate the $\text{GdMn}_{1-x}\text{Cr}_x\text{O}_3$ series.

In this paper we present systematic structural, electronic and magnetic investigations of the solid solutions, $\text{GdMn}_{1-x}\text{Cr}_x\text{O}_3$ ($0 \leq x \leq 1$). Doping GdMO_3 ($M = \text{Mn}/\text{Cr}$) gives rise to M -valence mixing and local static distortions around the doping ion, resulting in average lattice distortions in the compound. However, at considerable Cr-doping, the distortion is negligible resulting in a crossover from JT active region to JT inactive region.

II. EXPERIMENTAL AND THEORETICAL DETAILS

Polycrystalline samples of Cr-doped gadolinium manganites, $\text{GdMn}_{1-x}\text{Cr}_x\text{O}_3$ ($0 \leq x \leq 1$) were prepared by solid-state synthesis technique as reported elsewhere¹⁸. The crystalline structure and phase purity of the solid solutions were confirmed by x-ray diffraction (XRD) measurements using Bruker D8 Advance X-ray diffractometer equipped with $\text{Cu } K_\alpha$ radiation. Rietveld refinements of the obtained powder XRD patterns were carried out using the FULLPROF program. Raman spectroscopy measurements were performed using a micro-Raman spectrometer (inVia, Renishaw, United Kingdom) with 514.5 nm excitation of an Ar^+ laser. Spectra were collected in the backscattering configuration using a thermoelectrically cooled CCD camera as the detector and a long working distance $50\times$ objective with a numerical aperture of 0.45 was used for the acquisition. Magnetization measurements were carried out using SQUID-VSM from Quantum Design US. The O K -edge x-ray absorption spectra were recorded in total electron yield (TEY) mode at the CIRCULARPOLARIZATION beamline at the Elettra synchrotron radiation facility.

Our theoretical calculations of the structural, electronic and magnetic properties were based on density functional theory, using generalized gradient approximation (GGA) with Perdew Burke Ernzerhof for solids (PBEsol)²⁷ parameterization for the exchange correlation potential, the projector augmented wave (PAW) method²⁸, and a plane-wave basis set, as implemented in the Vienna ab-initio simulation package (VASP)²⁹. The interaction between ions and electrons was approximated with PAW potentials, treating $3p$, $3d$ and $4s$ for Cr/Mn and $2s$ and $2p$ for O as valence electrons. For Brillouin zone sampling, we chose $12 \times 12 \times 8$ Monkhorst-Pack k -point mesh³⁰ and the wave-function was expanded in a basis set consisting of plane waves with kinetic energies less than or equal to 770 eV. Using these parameters, an energy convergence of less than 1 meV/formula unit (f.u.) was achieved. Structures were fully relaxed until residual HellmannFeynman (HF) forces were smaller than $0.001 \text{ eV}/\text{\AA}$ while maintaining the symmetry constraints of the given space group. Gd $4f$ electrons were treated as valence electrons for parent compounds. We performed calculations using different Hubbard U values up to 4 eV for Mn/Cr and 4 eV for Gd and results for $U = 3 \text{ eV}$ for Mn/Cr and 4 eV for Gd explained satisfactorily the experimental results, which would be explained in later section. In $\text{GdMn}_{0.5}\text{Cr}_{0.5}\text{O}_3$, Gd $4f$ electrons were assumed as core electrons to reduce the calculations time. Irrespective of this, the $4f$ states lie deep in energy and they are almost completely localized so that they do not affect other valence states³¹. To visualize the orbital ordering in GdMnO_3 , in addition to the global X, Y, Z orthorhombic frame a local frame specific to each Jahn-Teller-type distorted MnO_6 octahedron was defined choosing x, y, z along the middle, short, and long Mn-O axes, respectively³¹.

III. RESULTS AND DISCUSSION

Figure 1(a) depicts room temperature XRD patterns of the solid solutions $\text{GdMn}_{1-x}\text{Cr}_x\text{O}_3$ ($0 \leq x \leq 1$) along with the corresponding Rietveld refined patterns considering orthorhombic $Pbnm$ space group except for GdCrO_3 , which is fitted well using $Pna2_1$ space group¹⁴. The composition dependent evolution of the lattice parameters (a , b , and $c/\sqrt{2}$) and cell volume (V) in $\text{GdMn}_{1-x}\text{Cr}_x\text{O}_3$ are shown in Fig. 1(b). A remarkable decrease in the value of b -axis, accompanied with an increase of the c -axis value has been observed with increasing Cr-content, while the a -axis remains almost constant. This suggests that lattice degrees of freedom confined to the bc -plane are strongly affected by the substitution of Cr. Further, the decrease in the cell volume reveals that the c -axis elongation is dominated by the b -axis reduction. Such structural characteristics can not be explained by considering the ionic radii of Cr^{3+} ion (0.615 \AA) in place of Mn^{3+} ion (0.645 \AA) alone.

Hence a detailed Rietveld refinement of the XRD patterns were carried out and the composition-dependent variations of three M -O bonds ($M = \text{Mn/Cr}$) in the MO_6 octahedra, obtained from Rietveld refinements are shown in Fig. 2 (a), with l_x, l_y and l_z denoting bond lengths along the respective local axes discussed in experimental and theoretical details. The intrinsic octahedral distortion in the orthorhombic structure allows the short and long bonds to lie within the ab -plane and the intermediate bond length along the c -axis^{22,32}. The large differences among the three M -O bond-lengths in GdMnO_3 are correlated with the cooperative JT distortion of Mn^{3+} ion along with a contribution from intrinsic structural distortion. In contrast, GdCrO_3 exhibits a regular structure with similar bond lengths of l_x, l_y and l_z , consistent with the quenched JT distortion for Cr^{3+} ion. The local modes characterizing the JT distortion are defined as in-(ab) plane orthorhombic distortion, Q_2 [$= l_y - l_x$] and out-of-plane tetragonal-like distortions, Q_3 [$= (2l_z - l_x - l_y)/\sqrt{3}$]^{22,33,34}, which are illustrated in Fig. 2 (b). The large positive value of Q_2 in GdMnO_3 is associated with the cooperative JT distortion, which is along the b -axis and Q_3 with negative sign indicates that an out-of-plane distortion along the c -axis is competing with the JT distortion^{22,33}. This implies that the lattice deformation is primarily confined to the bc -plane sub-lattice. In addition, the larger magnitude of Q_2 over Q_3 also indicates that the increase of c -axis is largely overwhelmed by decrease of b -axis. Upon approaching towards GdCrO_3 the decrease of both Q_2 and Q_3 indeed reveal gradual decrease of both JT and tetragonal distortions. An intriguing slope crossover in both Q_2 and Q_3 around $x \sim 0.35$ (guided by the dotted lines in Q_2) indicates the suppression of long range structural distortion associated with local JT distortion at the Mn sites.

Further examination of the average octahedral distortion Δ_d [$= (1/6) \sum_{n=1-6} [(d_n - \langle d \rangle) / \langle d \rangle]^2$, where d_n ($\langle d \rangle$) is the individual (average) M -O bond length] (depicted in Fig. 2 (c)), shows a slope changeover around $x \sim 0.35$ (guided by the dotted lines), a characteristic of crossover from JT-active region to JT-inactive region.

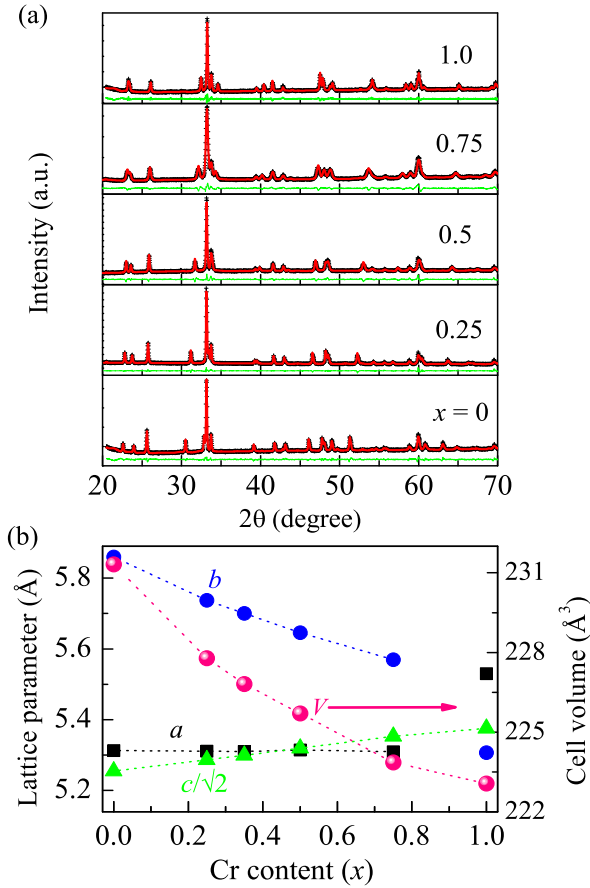


FIG. 1. (Color online) (a) The Rietveld-refinement plots of room temperature XRD patterns of $\text{GdMn}_{1-x}\text{Cr}_x\text{O}_3$ ($x = 0, 0.25, 0.5, 0.75$ and 1.0) in the space group of $Pbnm$. Experimental data is presented with symbol while the fitted curves from the Rietveld analysis are represented as red line. Difference spectra (difference between experimental data and fitting) is plotted in blue line. (b) Evolution of the cell parameters (a , b , and $c/\sqrt{2}$ (left panel) and cell volume (V) (right panel) as a function of compositions (x). As GdCrO_3 has $pnm2_1$ symmetry, lattice parameters a and b interchanges with respect to other compositions having $Pbnm$ symmetry.

JT-effect results in the lifting of degeneracy of e_g orbitals of Mn^{3+} ions and building up orbital ordering in the material. Thus, the JT distortion is conjugated with the ab -plane staggered orbital ordering. A polar plot of magnitude of the octahedral-site distortion, $\rho_0 (= Q_2^2 + Q_3^2)$ versus the angle ϕ ($= \tan^{-1}(Q_3/Q_2)$) was mapped for the compositions as shown in Fig. 2 (d), where ϕ opens from the Q_2 axis in anticlockwise direction³⁵.

The description of the e_g orbital associated with the M atom in an MO_6 octahedron can be made by the wave function ψ with a linear combination of orbitals $|x^2 - y^2\rangle$ and $|3z^2 - r^2\rangle$ in the (Q_2, Q_3) space as given by^{4,36}

$$\psi(\theta) = \cos(\theta/2) |3z^2 - r^2\rangle + \sin(\theta/2) |x^2 - y^2\rangle$$

where the angle θ ($\theta = 90^\circ + |\phi|$) represents respective orbital components, which opens anticlockwise from the Q_3 axis. The $\theta = 0, 2\pi/3$ and $4\pi/3$ correspond to orbitals $|3z^2 - r^2\rangle$, $|3y^2 - r^2\rangle$ and $|3x^2 - r^2\rangle$, respectively and $\theta = \pi/3, \pi$ and $5\pi/3$ represent $|y^2 - z^2\rangle$, $|x^2 - y^2\rangle$ and $|z^2 - x^2\rangle$, respectively. An octahedral site distortion, which has a θ deviating from these special angles reflects either the presence of orthorhombic distortion or a combination of orbital ordering and orthorhombic distortion. Figure 3 (b) depicts the schematic representation of orbital ordering in Mn^{3+} ions in GdMnO_3 . Since for all compositions in $\text{GdMn}_{1-x}\text{Cr}_x\text{O}_3$, θ falls between the special angle and close to $2\pi/3$ for one of the co-planer Mn-sites (site 1) as defined in Fig. 2 (e) (it is close to $4\pi/3$ for site 2), a new angle $\gamma = \pi/6 - \phi$ can be defined to simplify the wave functions for occupied (e_g^1) and unoccupied (e_g^2) orbitals for site 1, such that^{4,36}

$$\begin{aligned} \psi_{occ}(\gamma) &= \cos(\gamma/2) |3y^2 - r^2\rangle + \sin(\gamma/2) |z^2 - x^2\rangle \\ \psi_{unocc}(\gamma) &= -\sin(\gamma/2) |3y^2 - r^2\rangle + \cos(\gamma/2) |z^2 - x^2\rangle \end{aligned}$$

The total site distortion, as measured by ρ_0 , remains above 0.3 up to $x \sim 0.35$ compositions, reflecting a dominant contribution from a static JT orbital mixing along with the octahedral distortion^{4,36}. For $x = 0.5$ and higher compositions, ρ_0 is about one order of magnitude smaller than that of JT-active GdMnO_3 and other manganites (RMnO_3) and resembles the one found in JT-inactive rare-earth ferrites (RFeO_3) and vanadites (RVO_3) indicating the disappearance of orbital ordering^{4,33,36}.

To examine lattice anisotropy specific to the local Gd environment, nearest-neighbor Gd- M bond lengths are plotted, as shown in Fig. 4. There are eight NN-coordinated M which are doubly paired as $M1$ - $M4$, as viewed schematically in the inset of Fig. 3. Each pair of Gd- M lengths are equivalent for all compositions except GdCrO_3 , in which they are unequal (slightly) due to the $Pna2_1$ symmetry. The longest Gd- $M1$ (shortest Gd- $M4$) lying in the bc -plane, shows visible reduction (slight increase) towards $x = 1$, which is due to the suppression of JT distortion predominantly along the b -axis. The corresponding average local distortion, $\delta_d [= (1/8) \sum_{n=1-8} [(d_n - \langle d \rangle) / \langle d \rangle]^2]$, where d_n ($\langle d \rangle$) is the individual (average) Gd- M bond length] also shows a decrease of local anisotropy with increase of Cr-content followed by a slight increase in GdCrO_3 owing to having $Pna2_1$ symmetry. A slope change occurs (guided by dotted line) around the critical concentration, $x \sim 0.35$ of JT-crossover, consistent with earlier discussions. This suggests that the evolution of lattice and orbital degrees freedom in the solid solutions is also correlated with the bc -plane anisotropy in the local Gd-environment²².

In order to understand the lattice/atomic vibrations present in the above system and their role in the structural deformations, room temperature Raman spectroscopy measurements were performed in the solid solutions, as depicted in Fig. 4. For isostructural orthorhombic structure, the group theory predicts 24 Raman active modes ($7A_g + 7B_{1g} + 5B_{2g} + 5B_{3g}$) at the Γ point of the Brillouin zone^{14,37,38}, where as only 14 Raman active modes were observed. This may be because of the fact

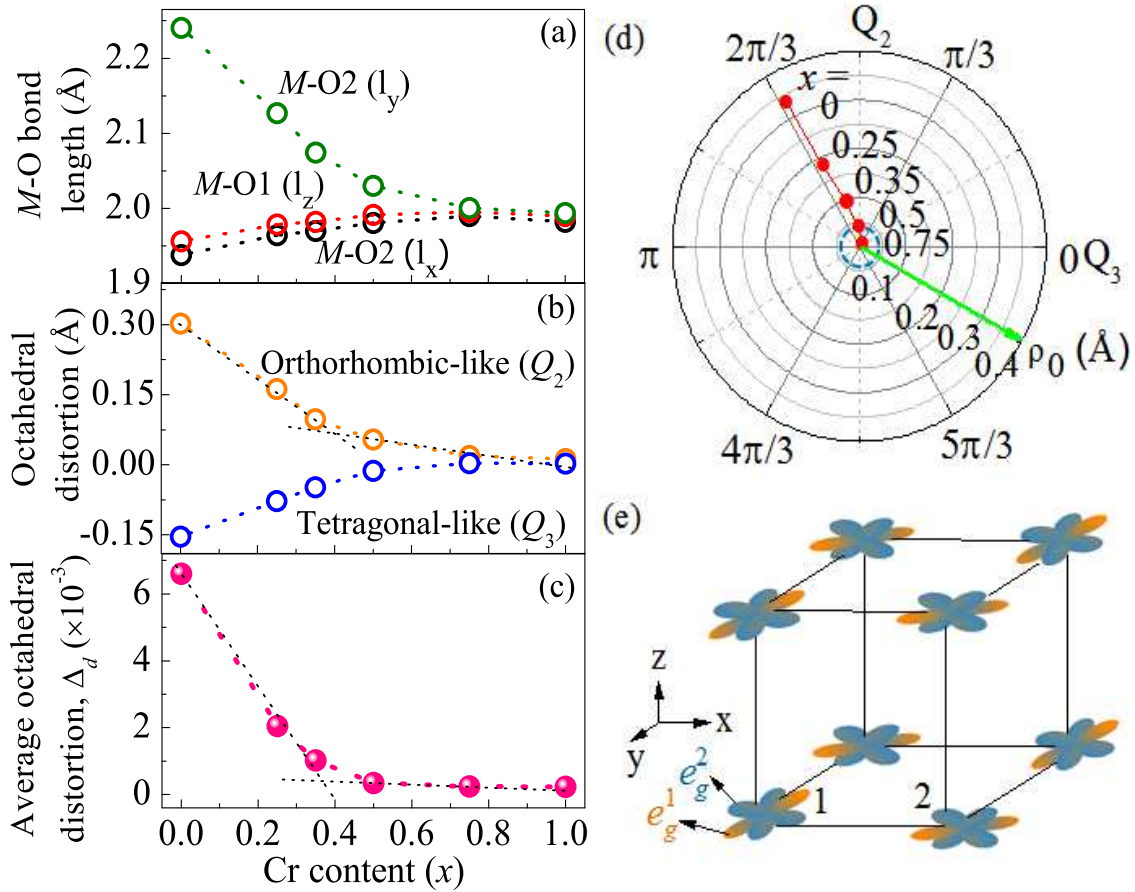


FIG. 2. (Color online) (a) The composition-dependent variations of the M -O bonds in the MO_6 octahedra of $GdMn_{1-x}Cr_xO_3$, with the long, short M -O2 bonds and the middle M -O1 bond, respectively. O1 (O2) represents the apical (equatorial) oxygen along the c -axis. (b) The composition-dependent variations of in- (ab) plane orthorhombic-like (Q_2) and out-of-plane tetragonal-like (Q_3) distortions. Dotted line guiding Q_2 point to the slope crossover around $x \sim 0.35$. (c) Variation of average octahedral distortion evaluated by Δ_d . Dotted lines guiding Δ_d to the slope crossover as a result of effective suppression of JT orbital ordering around $x \sim 0.35$. All the parameters are derived from the Rietveld refinements of the respective XRD patterns. (d) The polar plot of ρ_0 ($= Q_2^2 + Q_3^2$) and ϕ ($= \tan^{-1}(Q_3/Q_2)$), which are used to describe the orbital mixing in $GdMn_{1-x}Cr_xO_3$. (e) Schematic diagram of e_g orbitals of Mn^{3+} due to the JT orbital ordering.

that the other predicted modes are either too low in intensity or beyond our experimental range to be observed. The details about the observed modes are described elsewhere^{14,26,37,38}. The modes around 670 cm^{-1} may be the disorder-induced phonon density of states of oxygen vibrations^{39,40}. Apart from this, Kovaleva *et al.* argued that there is an additional component to the multi-order scattering, may arise from coupling between the low-energy electronic motion and the vibrational modes⁴¹.

The most common distortion in orthorhombic $Pbnm$ structure is the tilting of BO_6 octahedra, which can be described either by orthogonal tilt angles (leading to the $a^-a^-c^+$ Glazer's notation) or by octahedral tilts θ , ϕ and Φ around the pseudocubic $[110]_{pc}$ and $[001]_{pc}$ and $[111]_{pc}$ axis^{3,42-44}. The Raman modes, $A_g(3)$ and $A_g(5)$ are correlated with the tilt angles ϕ and θ , respectively^{37,43}. The position of $A_g(3)$ remains unchanged throughout the series i.e. ϕ remains constant. In contrast, $A_g(5)$ shows hardly any shift up to x

~ 0.5 compositions and thereafter, it shifts around 15 cm^{-1} towards high frequency for $x = 0.75$ and 1.0 compositions. This, in turn, suggests that θ remains more or less constant up to $x \sim 0.5$ compositions and slightly increase (negligibly small) for $x = 0.75$ and 1.0 compositions. Furthermore, Φ is correlated with θ and ϕ via the relation, $\cos\Phi = \cos\theta \cos\phi$ ^{42,43}, implying that Φ also increases slightly for $x = 0.75$ and 1.0 compositions. The in-plane antisymmetric stretching [$A_g(7)$] and symmetric stretching [$B_{1g}(7)$] modes are the JT modes, which are associated with the M -O2 bond lengths in ab -plane. The variation of frequency of these modes follows the relation, $\omega \propto d_{M-O2}^{-1.5}$ ^{37,45}, as shown in the inset of Fig. 4. $A_g(7)$ and $B_{1g}(7)$ modes show a clear shift up to $x \sim 0.5$ composition. Previously parameters extracted from the XRD patterns, depicted in Fig. 2, shows a rapid decrease of M -O2 bond length with Cr doping up to $x \sim 0.5$, suggesting that the clear shift in modes are arising from the rapid decrease of M -O2 bond length. Beyond $x \sim 0.5$ composition, both the

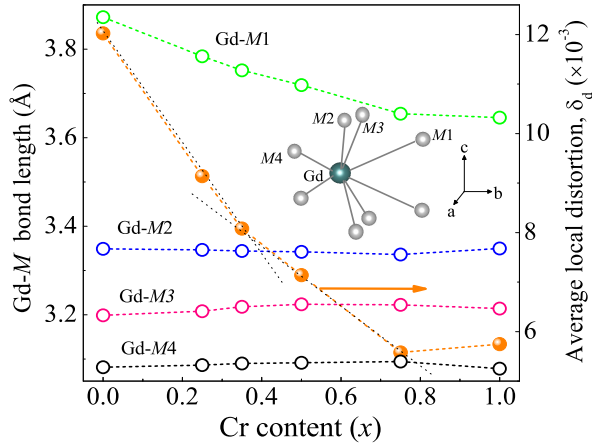


FIG. 3. (Color online) The evolution of the lattice anisotropy specific to the local Gd environment through variations in the nearest-neighbor Gd- M bond lengths. Right panel represents corresponding average distortion (δ_d) in the local Gd- M environment. Dotted lines guiding δ_d signify the slope crossover around $x \sim 0.35$. Inset represents nearest-neighbor Gd- M bond lengths with blue atom, Gd and gray atoms, M . All the parameters are derived from the Rietveld refinements of the respective XRD patterns.

variation in M -O2 bond length as well as the shift in modes become lesser suggesting their strong interdependence. With Cr-doping there is a rapid decrease of M -O2 bond length up to $x \sim 0.5$ (Fig. 2) leading to clear shift of these two modes after that shift is less. Furthermore, the spectral weight also decreases dramatically with increase of Cr-content (x) due to the reduction of JT distortion and becomes weak for .75 and 1.0 compositions, which are the JT-inactive compounds.

X-ray absorption spectroscopy (XAS) measurements were performed at the O K -edge of the solid solutions for $x = 0, 0.25, 0.5, 0.75$ and 1 to obtain information about the unoccupied $M 3d$, Gd $5d$ and deep Gd/ M states via the hybridization with the O $2p$ states^{22,46}, see Fig. 5 (a). Density of state (DOS) calculations were performed on the end compositions GdMnO₃ ($x = 0$) and GdCrO₃ ($x = 1$) and their total and site decomposed DOS are shown in Fig. 5 (b) and (c), respectively. Due to JT orbital ordering, the $e_g \uparrow$ band splits into two sub-bands: occupied $e_g \uparrow$ mainly dominated by $|3y^2 - r^2\rangle$ with a small contribution from $|z^2 - x^2\rangle$ and unoccupied $e_g \uparrow$, mainly contributed by $|z^2 - x^2\rangle$ mixing with $|3y^2 - r^2\rangle$ for one of the co-planar Mn sites (for other co-planar Mn sites, these two e_g orbitals are a mixture of $|3x^2 - r^2\rangle$ and $|y^2 - z^2\rangle$), as discussed earlier. Based on the DOS calculations, it can be deciphered that the features between 526.5-531 eV in the O K -edge spectra of GdMnO₃ are contributed by unoccupied $e_g \uparrow$ ($e_g^2 \uparrow$), $t_{2g} \downarrow + e_g \downarrow$ and $e_g \downarrow$ ^{22,46,47}, as labeled in Fig. 5 (a). The first peak around 527.8 eV arises from $e_g^2 \uparrow$ states. From the partial density of state (Fig. 6(b)), a band gap of 1.2 eV is obtained between these JT-split Mn $e_g \uparrow$ bands, which is in agreement with the calculated indirect band gap from absorption study of polycrystalline GdMnO₃⁴⁸. The second peak of XAS spectrum

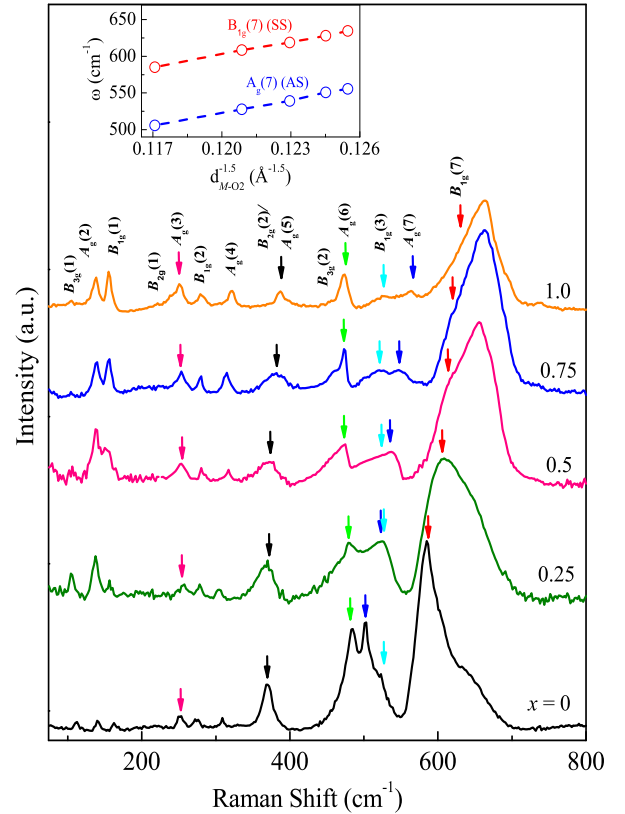


FIG. 4. (Color online) (a) Evolution of room temperature Raman spectra with compositions (x) in GdMn_{1-x}Cr_xO₃ ($x = 0, 0.25, 0.5, 0.75$ and 1.0). The inset shows the linear dependence of the JT symmetric stretching [$B_{2g}(7)$] and antisymmetric stretching [$A_g(7)$] modes frequency with the $d_{M-O_2}^{1.5}$, where d_{M-O_2} is the average of short and long M -O2 bond lengths.

around 529 eV is associated with $t_{2g} \downarrow$ and $e_g \downarrow$ states, with a small contribution from $e_g \downarrow$ around 530.5 eV. Further there is a splitting of 1.4 eV between $e_g^2 \uparrow$, $t_{2g} \downarrow + e_g \downarrow$ states, which agrees satisfactorily with the calculations.

In contrast to GdMnO₃, the O K -edge for the JT-inactive GdCrO₃ shows a single peak between 529-531 eV contributed by all unoccupied states of Cr³⁺ i.e. $e_g \uparrow$, $t_{2g} \downarrow$ and $e_g \downarrow$ states and is in good agreement with the calculated PDOS (Fig. 5 (c)). The energy gap of 2.7 eV obtained from the calculation agrees well with the experimentally obtained band gap values reported in chromite family^{49,50}. Above studies suggest that the first hump (527.8 eV) in XAS spectra for intermediate compositions generally arise from contribution of $e_g^2 \uparrow$ state of Mn-atoms and second broad hump contributes from $e_g \uparrow$ state of Cr and $t_{2g} \downarrow$ and $e_g \downarrow$ state of both Mn and Cr ions. A gradual decrease of the first peak with increasing of Cr composition is clearly observed.

The broad feature between 531-537 eV (Fig. 5 (a)) corresponds to Gd $5d$ states, indicating hybridization of Gd $5d$ and $M 3d$ ($e_g \uparrow$) states through the mediation of oxygen, suggesting Gd($4f$)- $M(3d)$ electronic interactions in these

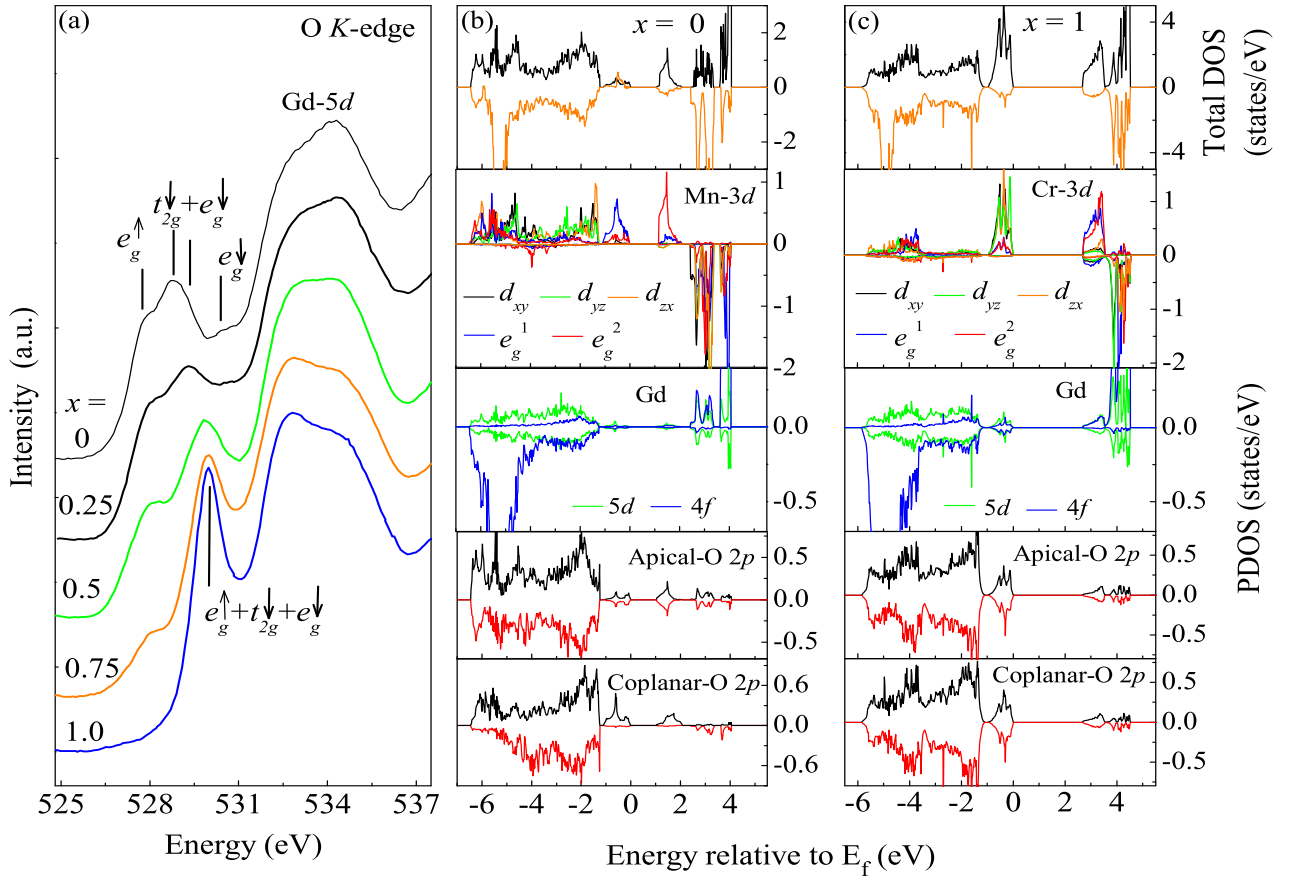


FIG. 5. (Color online) (a) Evolution of O K -edge XAS spectra with compositions (x) in $\text{GdMn}_{1-x}\text{Cr}_x\text{O}_3$ ($x = 0, 0.25, 0.5, 0.75$ and 1.0). (b) and (c) The total and site-decomposed DOS of GdMnO_3 and GdCrO_3 , respectively.

compounds^{51,52}. Owing to the highly localized character of the $4f$ states, direct $3d(M)-4f(\text{Gd})$ coupling is unlikely. Hence the interactions occur via $5d$ states as they are partially polarized by the $4f$ electrons via intra-atomic $4f-5d$ exchange interactions and finally couples with the $M-3d$ states mediated by the $\text{O}-2p$ states^{51,52}. The $3d-4f$ interactions via hybridized $5d$ and $\text{O}-2p$ states is also evidenced from the calculated DOS of GdMnO_3 and GdCrO_3 (Fig. 5 (b) and (c)). Temperature dependent magnetization measurements were performed on the solid solutions, $\text{GdMn}_{1-x}\text{Cr}_x\text{O}_3$, for $0 \leq x \leq 1$. Figure 6 depicts variation in magnetic moment at 10 K with doping concentration and insets represent temperature dependent magnetization measured in field-cooled-cooling (FCC) mode for various x values as indicated. Due to the co-operative JT orbital ordering in GdMnO_3 , NNN-AFM coupling plays a significant role in addition to NN-FM coupling in the ab -plane. There exists an AFM coupling between these layers along the c -axis. The competition between these leads to sinusoidal ordering below 40 K followed by canted A -type ($A_y F_z$ in Bertaut's notation) ordering below 20 K in Mn-sublattice as described in detail in our earlier report¹⁸. Remarkably, magnetization at low temperature (10 K) increases gradually upon Cr-doping up to $x \sim 0.25$ in

TABLE I. Calculated relative energies (E , in meV/unit cell) of various magnetic structures of $\text{GdMn}_{0.5}\text{Cr}_{0.5}\text{O}_3$. The unit cell contains two Mn and two Cr spins. The energies of the FM phase with layer-by-layer arrangements is used as the reference energy. Subscripts m and 'c' represent Mn and Cr ions, respectively.

Magnetic structure	$c\uparrow c\uparrow$ $m\uparrow m\uparrow$	$c\downarrow c\uparrow$ $m\uparrow m\uparrow$	$c\downarrow c\downarrow$ $m\uparrow m\uparrow$	$c\uparrow c\downarrow$ $m\downarrow m\uparrow$	$c\uparrow c\downarrow$ $m\uparrow m\downarrow$
E	0	-16.15	12.25	131.02	125.33
Magnetic structure	$m\uparrow c\uparrow$ $m\uparrow c\uparrow$	$m\uparrow c\downarrow$ $m\uparrow c\uparrow$	$m\downarrow c\uparrow$ $m\uparrow c\uparrow$	$m\downarrow c\downarrow$ $m\uparrow c\uparrow$	
E	354.87	332.98	420.76	421.31	
Magnetic structure	$c\uparrow m\uparrow$ $m\uparrow c\uparrow$	$c\downarrow m\downarrow$ $m\uparrow c\uparrow$	$c\uparrow m\downarrow$ $m\uparrow c\uparrow$	$c\downarrow m\uparrow$ $m\uparrow c\downarrow$	
E	321.31	306.16	343.92	372.3	

spite of the fact that Cr^{3+} moment is smaller than the Mn^{3+} moment, indicating the strengthening of FM interactions in the system. This is probably due to the increase in the strength of NN-FM coupling as compared to NNN-AFM

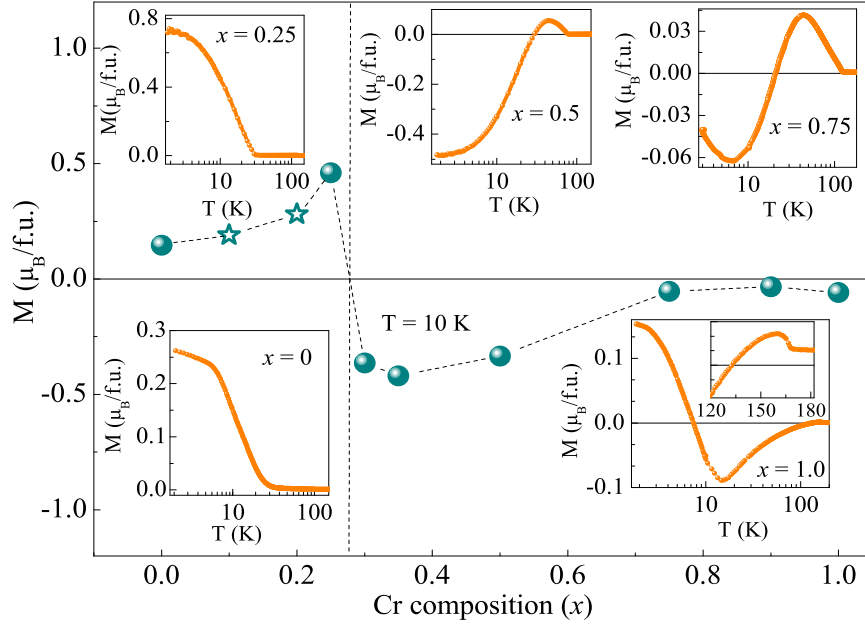


FIG. 6. (Color online) Variation in magnetic moment at 10 K with compositions (x) in $\text{GdMn}_{1-x}\text{Cr}_x\text{O}_3$. Stars (*) represent the results extracted from Ref. 21. Insets represent temperature dependent magnetization measured in field-cooled-cooling protocol of the solid solutions for $x = 0, 0.25, 0.5, 0.75$ and 1.

coupling in Mn-sublattice caused by progressive decrease of JT distortion. Furthermore, possibility of having magnetic interactions, probably FM in nature, between the Mn^{3+} and Cr^{3+} ions, can not be ignored, since such Mn^{3+} - Cr^{3+} FM coupling are reported previously in other Mn-Cr systems like $\text{TbMn}_{1-x}\text{Cr}_x\text{O}_3$ ²⁶, $\text{LaMn}_{1-x}\text{Cr}_x\text{O}_3$ ⁵³ and $\text{YMn}_{1-x}\text{Cr}_x\text{O}_3$ ⁵⁴ systems. The interaction between two Cr^{3+} moments may be ignored in this doping regime because of low Cr concentration. In GdCrO_3 , Cr^{3+} ions have t^3e^0 cubic-field d -electron configurations, which leads to an isotropic t^3 - O - t^3 AFM interactions resulting in canted G -type ordering (G_xF_z in Bertaut's notation) in Cr-sublattice below 169 K. The detailed magnetic interactions in GdCrO_3 is reported elsewhere¹⁵. In Cr-rich compositions Cr^{3+} - Cr^{3+} interactions dominate, thus have similar behavior to that of GdCrO_3 having a G -type magnetic structure. The canted spin structures in these systems is a direct consequence of antisymmetric Dzyaloshinskii-Moriya (DM) interaction [$D \cdot (\vec{S}_i \times \vec{S}_j)$]⁵⁵. Notably, FCC magnetization curve for $x = 0$ and 0.25 compositions show positive magnetization in the entire temperature region. However, one sees a magnetization reversal effect for all other compositions suggesting the strengthening of AFM coupling between Gd and M sublattices with increasing Cr-content. This magnetization reversal as a function of temperature above a critical Cr concentration suggests that there is a strong correlation between the structural distortion and magnetic coupling.

DFT calculations were performed to determine the possible low temperature magnetic ground state in $\text{GdMn}_{0.5}\text{Cr}_{0.5}\text{O}_3$.

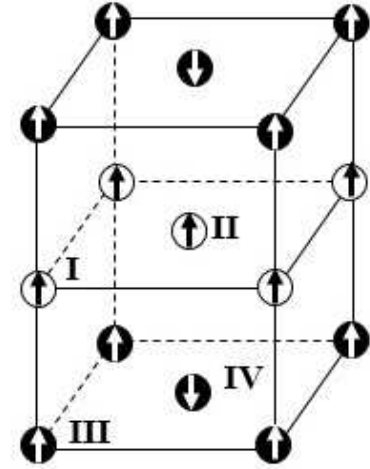


FIG. 7. (Color online) The calculated most stable magnetic structures in one unit cell for $\text{GdMn}_{0.5}\text{Cr}_{0.5}\text{O}_3$. Only the transition-metal ions Mn and Cr are shown (Filled circles: Mn; Empty circles: Cr). The ions labeled as I, II, III and IV are the non-equivalent atoms in the unit cell.

Previously reports on similar Mn-Cr systems with composi-

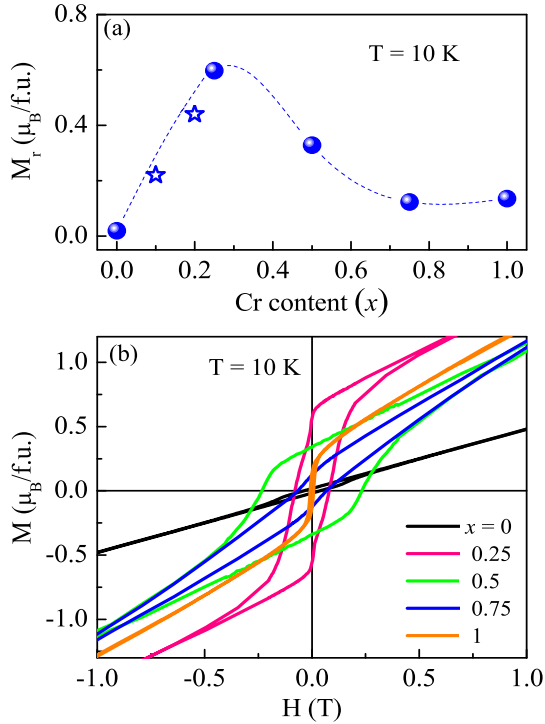


FIG. 8. (Color online) (a) Variation of remnant magnetization (M_r) at 10 K with compositions (x). Stars (*) represent the results extracted from Ref. 21 (b) Enlarged view of M - H loops measured at 10 K of the solid solutions for $x = 0, 0.25, 0.5, 0.75$ and 1.

tion $RMn_{0.5}Cr_{0.5}O_3$ suggest that the magnetic interactions in these systems strongly depend on the R -sites. For e.g., $TbMn_{0.5}Cr_{0.5}O_3$ exhibits G -type magnetic structure with the alternate arrangements of Mn and Cr atoms as confirmed from neutron diffraction study and DFT calculations⁵⁶. $DyMn_{0.5}Cr_{0.5}O_3$ has random distributions of Mn and Cr ions, which leads to two distinct magnetic orderings associated with $Cr^{3+}-Cr^{3+}$ and $Cr^{3+}-Mn^{3+}$ interactions as clearly seen in temperature dependent magnetization data⁵⁷. From DFT calculations, $LaMn_{0.5}Cr_{0.5}O_3$ was found to have stable structure with the layer-by-layer doping type (Mn and Cr are alternatively arranged along the c -axis). The DFT calculations also showed FM interactions between Mn ions and AFM interactions between Cr ions in the ab -plane and satisfactorily explained its magnetization⁵⁸. All the compounds discussed above possess $Pbnm$ symmetry. On the contrary, $YMn_{0.5}Cr_{0.5}O_3$ has monoclinic structure with layer-by-layer arrangements of Mn and Cr along the c -axis and exhibits ferrimagnetic behavior^{59,60}. In the present system $GdMn_{0.5}Cr_{0.5}O_3$, Reitveld refinement of XRD pattern using orthorhombic $Pbnm$ structure showed better fitting than that of the monoclinic structure. Also temperature dependent magnetization measurements did not show double transitions like in $DyMn_{0.5}Cr_{0.5}O_3$, implying that Mn and Cr are well ordered.

To understand the magnetic coupling in $GdMn_{0.5}Cr_{0.5}O_3$, the total energy was calculated within the framework of GGA including Hubbard U , for various possible arrangements of Mn and Cr ions and various possible spin configurations, as listed in Table I. The results of GGA+ U are consistent with the results including spin-orbital coupling (SOC) i.e. GGA+ U +SOC as reported in $TbMn_{0.5}Cr_{0.5}O_3$ ⁵⁶. It is found that structure with the layer-by-layer doping type with a FM interaction between Mn^{3+} spins and AFM interaction between Cr^{3+} spins is the most stable configuration similar to that of $LaMn_{0.5}Cr_{0.5}O_3$ ⁵⁸.

In constructing an effective Spin Hamiltonian (SH) to understand the spin dependent energetics of $GdMn_{0.5}Cr_{0.5}O_3$ only Mn^{3+} and Cr^{3+} spins were considered, since Gd^{3+} spins were not included in the total energy calculations. The unit cell used in the calculation of the energies for different Mn and Cr arrangements and different spin orientations consists of 20 atoms, $Gd_4Mn_2Cr_2O_{12}$, consisting of two Mn and two Cr ions. The unit cell then consists of 4 magnetic atoms I-IV; I, II are in one basal plane representing the Mn atoms and III, IV are in the other basal plane representing the Cr atoms as shown schematically in Fig. 7. The structure in the figure is denoted as $(Mn\uparrow, Mn\uparrow)(Cr\uparrow, Cr\downarrow)$, which is the lowest energy atomic structure obtained from the calculations.

The SH for the system is given by

$$H_{spin} = -J_1 \sum_{\langle ij \rangle l} \vec{S}_{il}^{Mn} \cdot \vec{S}_{jl}^{Mn} - J_2 \sum_{\langle ij \rangle l} \vec{S}_{il}^{Cr} \cdot \vec{S}_{jl}^{Cr} - J_3 \sum_{\langle ll' \rangle l} \vec{S}_{il}^{Mn} \cdot \vec{S}_{il'}^{Cr} + \Delta \quad (1)$$

where i, j indicate lattice sites in the basal (ab) plane and l indicates different layers along the c axis. The number of Mn-Mn bonds Cr-Cr bonds and Mn-Cr bonds per unit cell are four each, as presented in Fig. 8. There are four parameters in the SH which were estimated using calculated DFT energies for different spin configurations with layer-by-layer arrangements of Mn and Cr along the c -axis (see Table I first row). Here $S^{Mn}=2$; $S^{Cr}=3/2$. In the mean-field approximation, energy/unit-cell (in meV/unit cell) for four different spin configurations are given below. Energy for a fifth configuration can be predicted within SH model and compared with DFT energy.

$$E_I = -16J_1 - 9J_2 - 12J_3 + \Delta = 0 \quad (2)$$

$$E_{II} = -16J_1 + 9J_2 + \Delta = -16.15 \quad (3)$$

$$E_{III} = -16J_1 - 9J_2 + 12J_3 + \Delta = +12.25 \quad (4)$$

$$E_{IV} = +16J_1 + 9J_2 + 12J_3 + \Delta = +131.02 \quad (5)$$

$$E_V = +16J_1 + 9J_2 - 12J_3 + \Delta \quad (6)$$

The Eqs. 2-5 can be solved to give: $J_1 = J^{Mn-Mn} = 4.39$ meV (Ferro), $J_2 = J^{Cr-Cr} = -1.26$ meV (Antiferro), $J_3 = J^{Mn-Cr} = 0.55$ meV (Ferro) and $\Delta = 65.48$ meV. Using these parameters $E_V = 117.78$ meV can be predicted, whereas the calculated DFT energy is 125.33 meV. Looking at the calculated exchange parameters, the coupling between Mn spins is ferromagnetic and strong, similar to the parent manganite, i.e. $GdMnO_3$. The coupling between Cr spins is antiferromagnetic, again similar to the parent compound $GdCrO_3$. The cross coupling between Mn and Cr spin is ferromagnetic and weak. Earlier report on transport studies in $LaMn_{1-x}Cr_xO_3$; $0 \leq x \leq 0.15$. argues that the experimental findings could be understood through a simple model of the electronic structure of the alloy, which included FM double exchange interaction between Mn and Cr spins and a CPA type approximation to handle disorder⁶¹. It is possible that the small magnitude of J^{Mn-Cr} results from a near cancellation between two competing contributions, one the usual AFM super-exchange and the other FM double exchange.

Figure 8 (a) and (b) shows the variation of the remnant magnetization (M_r) at 10 K for $GdMn_{1-x}Cr_xO_3$ for various x values and their corresponding M - H loops are shown in , respectively. M_r shows a non-monotonic variation with composition: initially it increases with increasing Cr concentration (x) and reaches a maximum value for $x \sim 0.3$. Beyond $x \sim 0.3$, M_r starts decreasing for increasing in x followed by no distinct variation beyond $x \sim 0.7$. As discussed previously, magnetic behavior in the solid solution is a combination of variety of magnetic interactions such as symmetric exchange interactions (FM and AFM type) and antisymmetric DM interaction coupled to octahedral tilting. The DM interaction is directly proportional to the perpendicular displacement of oxygen in the M -O- M chain, which, in turn, depends on the tilt angles^{62,63}. It is evident from Raman spectroscopy data that there is hardly any change of tilt angles throughout the series, suggesting that the contributions from canted ferromagnetism (DM interaction) remains almost constant throughout the series. Thus, the increase of M_r up to $x \sim 0.3$ suggests an increase of NN-FM coupling as compared to NNN-AFM coupling caused by the progressive decrease of JT-orbital or-

dering and incorporation of Mn^{3+} - Cr^{3+} FM interactions as discussed earlier. Beyond $x \sim 0.3$ ferrimagnetic type structure arises due to the incorporation of AFM Cr^{3+} - Cr^{3+} interactions, thus resulting in decrease of M_r . In Cr-rich compositions ($x \geq 0.7$), AFM Cr^{3+} - Cr^{3+} interactions are more dominating resulting in no further change in M_r .

IV. CONCLUSION

The structural, electronic and magnetic properties of $GdMn_{1-x}Cr_xO_3$ were studied. In the structural investigations, it was found that the JT distortion characteristic to Mn^{3+} results in bond anisotropy and effective orbital ordering for $x \leq 0.35$. A gradual variation of electronic states with doping is also clearly seen in O- K edge x-ray absorption spectra. The temperature dependence of magnetization under the FCC mode shows sign reversal effect for $x \geq 0.35$, whereas magnetization does not change sign in the JT-active region. The change in magnetic polarity at the critical concentration coinciding with JT-crossover, infers a complex interplay of magnetic interaction and structural distortion. The nonmonotonic variation of remnant magnetization can be explained in terms of doping induced modification of symmetric magnetic interactions (FM/AFM type). DFT calculations using GGA+U type exchange correlation potential find that the system with $x = 0.5$ consists of alternate ferromagnetic Mn layers and antiferromagnetic Cr layers. The strength of the ferromagnetic exchange interaction between nearest neighbor Mn spins is stronger than the NN Cr antiferromagnetic exchange. The exchange interaction between NN Mn and Cr is quite small but ferromagnetic. This is distinctly different from that observed for both end members $GdMnO_3$ and $GdCrO_3$.

V. ACKNOWLEDGMENT

B. R. would like to thank Prof. P. V. Satyam, IOP, Bhubaneswar, India for computational facilities.

† Present address: Rajdhani College, Baramunda Square, Nayapalli, Bhubaneswar - 751003, Odisha, India.

* dinesh.topwal@iopb.res.in, dinesh.topwal@gmail.com

¹ R. H. Mitchell, *Perovskites: Modern and Ancient* (2002).

² A. Glazer, *Acta Cryst.* **28**, 3384 (1972).

³ A. Glazer, *Acta Cryst.* **31**, 756 (1975).

⁴ J.-S. Zhou and J. Goodenough, *Physical review letters* **96**, 247202 (2006).

⁵ C. N. R. Rao and B. Raveau, *Colossal magnetoresistance, charge ordering and related properties of manganese oxides* (World Scientific, 1998).

⁶ S. Mori, T. Katsufuji, N. Yamamoto, C. Chen, and S. Cheong, *Physical Review B* **59**, 13573 (1999).

⁷ J. van den Brink, G. Khaliullin, and D. Khomskii, *Physical Review Letters* **83**, 5118 (1999).

⁸ T. Asaka, S. Yamada, S. Tsutsumi, C. Tsuruta, K. Kimoto, T. Arima, and Y. Matsui, *Physical review letters* **88**, 097201 (2002).

⁹ H. Kawano, R. Kajimoto, H. Yoshizawa, Y. Tomioka, H. Kuwahara, and Y. Tokura, *Physical Review Letters* **78**, 4253 (1997).

¹⁰ N. Fukumoto, S. Mori, N. Yamamoto, Y. Moritomo, T. Katsufuji, C. Chen, and S. Cheong, *Physical Review B* **60**, 12963 (1999).

¹¹ M. Mochizuki and N. Furukawa, *Physical Review B* **80**, 134416 (2009).

¹² S.-W. Cheong and M. Mostovoy, *Nat. Mater.* **6**, 13 (2007).

¹³ B. Rajeswaran, D. Khomskii, A. Zvezdin, C. Rao, and A. Sundaresan, *Physical Review B* **86**, 214409 (2012).

¹⁴ S. Mahana, B. Rakshit, R. Basu, S. Dhara, B. Joseph,

- U. Manju, S. D. Mahanti, and D. Topwal, *Physical Review B* **96**, 104106 (2017).
- ¹⁵ S. Mahana, U. Manju, and D. Topwal, in *AIP Conference Proceedings*, Vol. 1832 (AIP Publishing, 2017) p. 130046.
- ¹⁶ Y. Cao, S. Cao, W. Ren, Z. Feng, S. Yuan, B. Kang, B. Lu, and J. Zhang, *Applied Physics Letters* **104**, 232405 (2014).
- ¹⁷ M. El Amrani, M. Zaghrioui, V. T. Phuoc, F. Gervais, and N. E. Massa, *Journal of Magnetism and Magnetic Materials* **361**, 1 (2014).
- ¹⁸ S. Mahana, U. Manju, and D. Topwal, *J Physics D: Applied Physics* **50**, 035002 (2017).
- ¹⁹ T. Kimura, G. Lawes, T. Goto, Y. Tokura, and A. Ramirez, *Physical Review B* **71**, 224425 (2005).
- ²⁰ J. A. Moreira, A. Almeida, M. Chaves, J. Kreisel, J. Oliveira, F. Carpinteiro, and P. Tavares, *Journal of Physics: Condensed Matter* **24**, 436002 (2012).
- ²¹ A. Modi and N. Gaur, *J Alloys Compounds* **644**, 575 (2015).
- ²² F.-K. Chiang, M.-W. Chu, F. Chou, H. Jeng, H. Sheu, F. Chen, and C. Chen, *Physical Review B* **83**, 245105 (2011).
- ²³ Z. Long and W. Xiao-Shan, *Chinese Physics B* **22**, 107806 (2013).
- ²⁴ Y. Fang, Y. Yang, X. Liu, J. Kang, L. Hao, X. Chen, L. Xie, G. Sun, V. Chandragiri, C.-W. Wang, *et al.*, *Scientific reports* **6**, 33448 (2016).
- ²⁵ Y.-H. Huang, M. Karppinen, N. Imamura, H. Yamauchi, and J. B. Goodenough, *Physical Review B* **76**, 174405 (2007).
- ²⁶ M. Staruch and M. Jain, *J. Phys.: Condens. Matter* **26**, 046005 (2014).
- ²⁷ J. P. Perdew, A. Ruzsinszky, G. I. Csonka, O. A. Vydrov, G. E. Scuseria, L. A. Constantin, X. Zhou, and K. Burke, *Phys. Rev. Lett.* **100**, 136406 (2008).
- ²⁸ G. Kresse and D. Joubert, *Phys. Rev. B* **59**, 1758 (1999).
- ²⁹ G. Kresse and J. Furthmüller, *Phys. Rev. B* **54**, 11169 (1996).
- ³⁰ H. J. Monkhorst and J. D. Pack, *Phys. Rev. B* **13**, 5188 (1976).
- ³¹ K. Yamauchi, F. Freimuth, S. Blügel, and S. Picozzi, *Physical Review B* **78**, 014403 (2008).
- ³² J.-S. Zhou, J. Alonso, V. Pomjakushin, J. Goodenough, Y. Ren, J.-Q. Yan, and J.-G. Cheng, *Physical Review B* **81**, 214115 (2010).
- ³³ J.-S. Zhou and J. Goodenough, *Physical Review B* **77**, 132104 (2008).
- ³⁴ M. Tachibana, T. Shimoyama, H. Kawaji, T. Atake, and E. Takayama-Muromachi, *Physical Review B* **75**, 144425 (2007).
- ³⁵ J. Kanamori, *Journal of Applied Physics* **31**, S14 (1960).
- ³⁶ J.-S. Zhou and J. Goodenough, *Physical Review B* **77**, 172409 (2008).
- ³⁷ M. Iliev, M. Abrashev, J. Laverdiere, S. Jandl, M. Gospodinov, Y.-Q. Wang, and Y.-Y. Sun, *Physical Review B* **73**, 064302 (2006).
- ³⁸ N. Todorov, M. Abrashev, V. Ivanov, G. Tsutsumanova, V. Marinova, Y.-Q. Wang, and M. Iliev, *Physical Review B* **83**, 224303 (2011).
- ³⁹ M. Iliev, V. Hadjiev, A. Litvinchuk, F. Yen, Y.-Q. Wang, Y. Sun, S. Jandl, J. Laverdiere, V. Popov, and M. Gospodinov, *Physical Review B* **75**, 064303 (2007).
- ⁴⁰ M. Iliev, M. Abrashev, V. Popov, and V. Hadjiev, *Physical Review B* **67**, 212301 (2003).
- ⁴¹ N. N. Kovaleva, O. E. Kusmartseva, K. Kugel, A. Maksimov, D. Nuzhnyy, A. Balbashov, E. Demikhov, A. Dejneka, V. Trepakov, F. Kusmartsev, *et al.*, *Journal of Physics: Condensed Matter* **25**, 155602 (2013).
- ⁴² Y. Zhao, D. J. Weidner, J. B. Parise, and D. E. Cox, *Physics of the Earth and Planetary Interiors* **76**, 17 (1993).
- ⁴³ M. C. Weber, J. Kreisel, P. A. Thomas, M. Newton, K. Sardar, and R. I. Walton, *Physical Review B* **85**, 054303 (2012).
- ⁴⁴ L. M. Daniels, M. C. Weber, M. R. Lees, M. Guennou, R. J. Kashtiban, J. Sloan, J. Kreisel, and R. I. Walton, *Inorganic chemistry* **52**, 12161 (2013).
- ⁴⁵ L. Martín-Carrón, A. De Andres, M. Martínez-Lope, M. Casais, and J. Alonso, *Physical Review B* **66**, 174303 (2002).
- ⁴⁶ J. Chen, J. Lee, C. Chen, T. Chou, K. Lu, S. Haw, K. Liang, C. Chen, H. Jeng, S. Huang, *et al.*, *Applied Physics Letters* **94**, 044105 (2009).
- ⁴⁷ J. Chen, Z. Hu, H. Jeng, Y. Chin, J. Lee, S. Huang, K. Lu, C. Chen, S. Haw, T. Chou, *et al.*, *Physical Review B* **81**, 201102 (2010).
- ⁴⁸ S. Bukhari and J. Ahmad, *Acta Phys. Pol. A* **129**, 43 (2016).
- ⁴⁹ G. Kotnana and S. N. Jammalamadaka, *Journal of Applied Physics* **118**, 124101 (2015).
- ⁵⁰ P. Gupta and P. Poddar, *RSC Advances* **6**, 82014 (2016).
- ⁵¹ M. Richter, *Journal of Physics D: Applied Physics* **31**, 1017 (1998).
- ⁵² A. Stroppa, M. Marsman, G. Kresse, and S. Picozzi, *New Journal of Physics* **12**, 093026 (2010).
- ⁵³ U. Bents, *Physical Review* **106**, 225 (1957).
- ⁵⁴ S. Li, T. Wang, H. Han, X. Wang, H. Li, J. Liu, and J. Liu, *Journal of Physics D: Applied Physics* **45**, 055003 (2012).
- ⁵⁵ T. Moriya, *Physical Review* **120**, 91 (1960).
- ⁵⁶ M. Staruch, V. Sharma, C. dela Cruz, R. Ramprasad, and M. Jain, *Journal of Applied Physics* **116**, 033919 (2014).
- ⁵⁷ B. Yuan, J. Yang, X. Zuo, X. Kan, L. Zu, X. Zhu, J. Dai, W. Song, and Y. Sun, *Journal of Applied Physics* **118**, 124103 (2015).
- ⁵⁸ Z. Yang, L. Ye, and X. Xie, *Journal of Physics: Condensed Matter* **12**, 2737 (2000).
- ⁵⁹ L. Yang, Q. Duanmu, L. Hao, Z. Zhang, X. Wang, Y. Wei, and H. Zhu, *Journal of Alloys and Compounds* **570**, 41 (2013).
- ⁶⁰ L. Hao, L. Yang, M.-H. Lee, T.-H. Lin, Z. Zhang, X. Xie, and H. Zhu, *Journal of Alloys and Compounds* **601**, 14 (2014).
- ⁶¹ L. Morales, R. Allub, B. Alascio, A. Butera, and A. Caneiro, *Phys. Rev. B* **72**, 132413 (2005).
- ⁶² L. Bellaiche, Z. Gui, and I. A. Kornev, *Journal of Physics: Condensed Matter* **24**, 312201 (2012).
- ⁶³ A. Singh, A. Senyshyn, H. Fuess, S. J. Kennedy, and D. Pandey, *Physical Review B* **89**, 024108 (2014).